

ARTICLE

Received 17 Dec 2015 | Accepted 25 Feb 2016 | Published 15 Apr 2016

DOI: 10.1038/ncomms11230

OPEN

# Femtosecond electron imaging of defect-modulated phonon dynamics

Daniel R. Cremons<sup>1,\*</sup>, Dayne A. Plemmons<sup>1,\*</sup> & David J. Flannigan<sup>1</sup>

Precise manipulation and control of coherent lattice oscillations via nanostructuring and phonon-wave interference has the potential to significantly impact a broad array of technologies and research areas. Resolving the dynamics of individual phonons in defect-laden materials presents an enormous challenge, however, owing to the interdependent nanoscale and ultrafast spatiotemporal scales. Here we report direct, real-space imaging of the emergence and evolution of acoustic phonons at individual defects in crystalline WSe<sub>2</sub> and Ge. Via bright-field imaging with an ultrafast electron microscope, we are able to image the sub-picosecond nucleation and the launch of wavefronts at step edges and resolve dispersion behaviours during propagation and scattering. We discover that the appearance of speed-of-sound (for example, 6 nm ps<sup>-1</sup>) wavefronts are influenced by spatially varying nanoscale strain fields, taking on the appearance of static bend contours during propagation. These observations provide unprecedented insight into the roles played by individual atomic and nanoscale features on acoustic-phonon dynamics.

<sup>1</sup>Department of Chemical Engineering and Materials Science, University of Minnesota, 421 Washington Avenue SE, Minneapolis, Minnesota 55455, USA.  
\* These authors contributed equally to this work. Correspondence and requests for materials should be addressed to D.J.F. (email: flan0076@umn.edu).

**P**honons—quantized elastic oscillations—are at the core of innumerable atomic-scale physical processes and mesoscale phenomena, from structural variations associated with lattice fluctuations, phase transitions and bond modulation<sup>1–5</sup> to electromagnetic and electronic properties, including electric susceptibility and electron mobility<sup>6–10</sup>. Consequently, the atomic-scale manipulation and control of phonon modes has been proposed and vigorously pursued for enabling and enhancing myriad technological developments, including electromagnetic confinement in optically driven cavities<sup>11,12</sup> and, especially, thermal-energy management and conversion<sup>13–18</sup>. Achieving this requires a deep understanding of the profound influence that phonons have on emergent properties in both engineering and advanced materials through the fundamental structure–function relationships at work therein. As such, the formulation of a comprehensive microscopic description of the real-time interaction of propagating modes with individual lattice discontinuities would constitute a significant advance toward ultraprecise directed-energy nucleation and mode guiding in defect-laden materials.

Of particular interest is the development of a detailed understanding of phonon dynamics in nanostructured and disordered semiconducting materials (for example, SiGe alloys and composites)<sup>19–21</sup>, especially those having tunable band gaps, such as the layered transition metal dichalcogenides (for example, WSe<sub>2</sub>, MoS<sub>2</sub>, NbSe<sub>2</sub> and so on)<sup>5,6,9,10,22</sup>. These compounds have generated an enormous amount of interest owing to dramatic differences in, and tunability of, transport properties (thermal and electronic) along different crystallographic directions and with varying numbers of layers. For example, it was shown with WSe<sub>2</sub> that the cross-plane thermal conductivity could be made several times smaller than the predicted minimum value (indeed, the smallest measured for any fully dense solid) via disordering of the two-dimensional sheets<sup>23</sup>. This was attributed mainly to phonon localization stemming from the incommensurate nature of the individual crystalline WSe<sub>2</sub> planes, thus restricting these modes from significantly contributing to thermal transport.

To elucidate the dynamics of collective excitations in the presence of individual atomic-scale defects, one must contend with the difficult-to-access spatiotemporal regimes in which these phenomena operate. At the unit-cell level, speed-of-sound phonon wavefronts typically transit such spatial dimensions in less than 100 femtoseconds. The propagating energy causes local bond modulation and a transient elastic deformation of the lattice, briefly re-orienting the atoms in a manner dictated by the symmetry of the mode. Structural dynamics of this nature are amenable to study with ultrafast methods that make use of the dependence of scattering wavevectors on lattice orientation and symmetry<sup>24–28</sup>; movement or spacing and symmetry changes of the reciprocal lattice on a fixed Ewald sphere produces a commensurate modulation or re-configuration of the resulting coherent-scattering pattern. In reciprocal space, the dearth of phase information, combined with the probing of lattice motion within material volumes that are large relative to nanoscale discontinuities (for parallel-beam conditions), produces an ensemble-averaged picture of the dynamics, despite being sensitive to symmetry changes<sup>29–31</sup>, bond dilation and breaking<sup>2,3</sup> and atomic-vibration amplitude<sup>32–34</sup>. Conversely, phase information is retained with femtosecond electron imaging<sup>35–38</sup>, thus enabling spatiotemporal localization of discrete phonon-nucleation events and resolution of propagation dynamics at individual atomic-scale defects.

Here we report direct visualization of the nucleation, evolution and decay of individual acoustic phonons in the vicinity of atomic-scale defects and nanoscale variations in lattice orientation via femtosecond real-space imaging with an ultrafast electron microscope. Experimentally, we observe the launch

of individual phonon wavefronts following coherent optical excitation of macroscopically ordered but microscopically disordered materials: here, crystalline tungsten diselenide (WSe<sub>2</sub>) and germanium (Ge). The transient low-energy elastic deformations associated with the propagating waves produce a slight re-orientation of the lattice and thus a localized, rapidly varying Bragg condition. This manifests as coherent diffraction-contrast wavetrains in the real-space images, the nucleation and apparent dynamics of which are found to be strongly dictated by even minor lattice imperfections. Further, we observe that the appearance and directionality of the propagating wavefronts, as seen in the femtosecond bright-field images, are strongly influenced by individual step edges, interfaces and crystal bending. By isolating and quantifying the transient contrast modulation, we extract the spatially dependent vibrational-mode shapes and properties—namely, symmetries, frequencies, phase velocities and decay times—over fields-of-view on the order of the phonon wavelengths. These observations open the way to detailed study of the effects of individual atomic-scale defects, spatially varying lattice orientations and associated strain fields on ultrafast energy propagation in less-than-pristine materials.

## Results

**Overview of WSe<sub>2</sub> and Ge specimens.** To locate and characterize specific defects and other nanoscale imperfections of interest, the WSe<sub>2</sub> and Ge specimens were initially surveyed using bright-field imaging and parallel-beam electron diffraction. Static structural and morphological characterization of specific specimen regions of interest, on which subsequent femtosecond electron imaging studies were conducted, are summarized in Fig. 1. As can be seen from the diffraction patterns, the WSe<sub>2</sub> and Ge specimens are oriented such that the electron beam travels approximately down the [001] and [110] zone axes, respectively (Fig. 1c,f)<sup>39</sup>. Combined, the bright-field images and corresponding diffraction patterns illustrate the macroscopically crystalline but microscopically disordered nature of the regions. From the images, several features of interest for the present study can be identified, which, conversely, are not readily apparent from the diffraction patterns alone. These include step edges and terraces, wrinkles, folds, vacuum-crystal interfaces and cracks. In addition, bend contours are quite prominent and widespread, as are moiré fringes in the WSe<sub>2</sub> specimen. See the ‘Methods’ section below for descriptions of how the specimens were prepared.

**Imaging acoustic-phonon wavefronts and wavetrains.** With the applied experimental conditions (stroboscopic femtosecond electron microscopy; see ‘Methods’ section), propagating periodic-contrast modulation arising from femtosecond optical excitation was observed in both the specimens (Fig. 2). Owing to the challenge of conveying the behaviour of the observed acoustic-phonon dynamics within a series of static images, the reader is strongly encouraged to view Supplementary Videos 1 through 6, within which the dynamics are striking and more readily apparent. In addition, Supplementary Fig. 1 comprises the same images as shown in Fig. 2, but the display method is different in order to provide additional perspective. From the sequence of femtosecond electron images, phase velocities of 6.5 and 5.5 nm ps<sup>−1</sup>, commensurate periodicities of 40 and 44 ps, and GHz frequencies (Supplementary Fig. 2) were determined for the travelling contrast modulations in Ge and WSe<sub>2</sub>, respectively. This was accomplished by analysing oscillations in the image intensity as a function of both space and time (Fig. 2h,p; see ‘Methods’ section). The close correspondence of the phase velocities to the bulk, in-plane speed of sound indicates the contrast dynamics arise from propagating acoustic phonons—

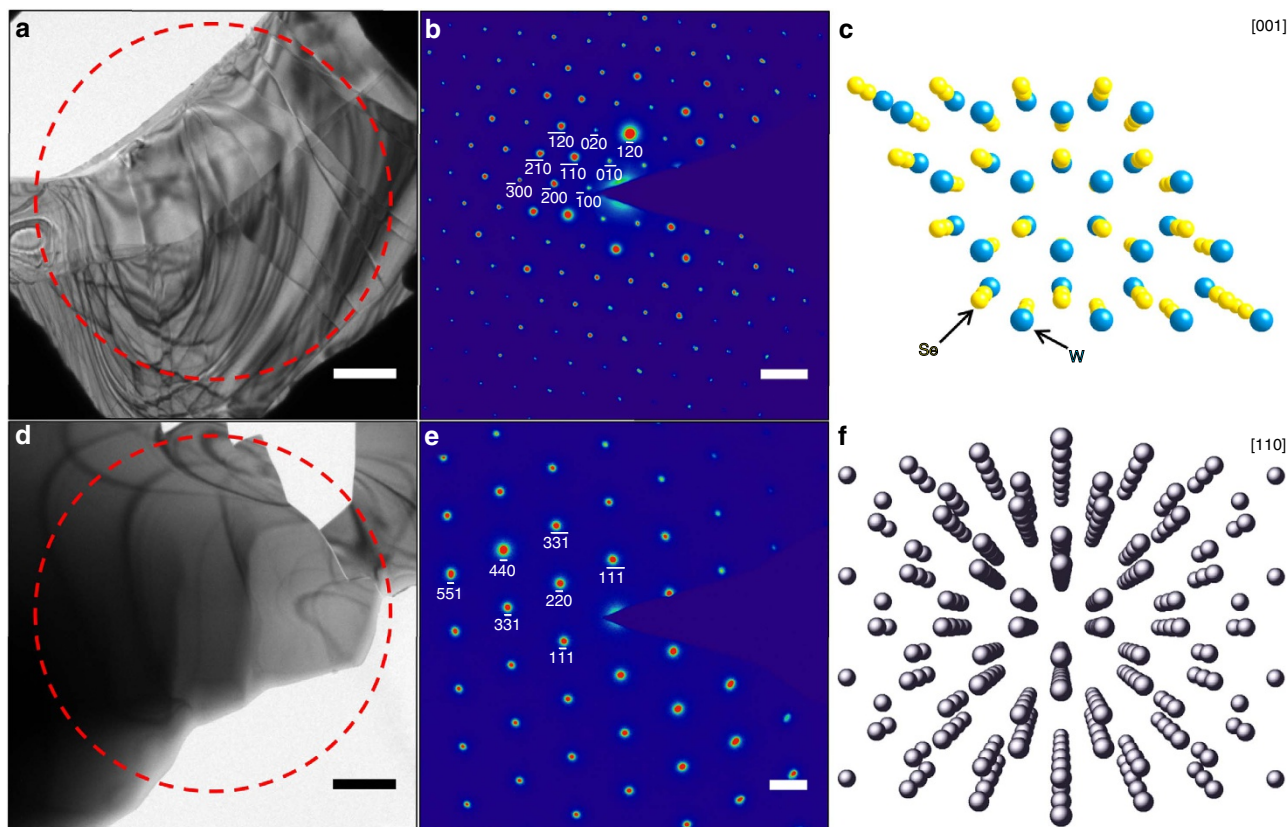


**Figure 1 | Morphological heterogeneity and atomic-scale order of the WSe<sub>2</sub> and Ge specimen regions of interest.** (a,d) Bright-field images of (a) a WSe<sub>2</sub> flake and (d) a thin Ge crystal. The red, dashed circle denotes the position of the selected-area aperture used to generate the diffraction patterns shown in b and e. Scale bars, 1  $\mu\text{m}$ . (b,e) Corresponding selected-area diffraction patterns obtained approximately along the [001] and [110] zone axes for WSe<sub>2</sub>, and Ge, respectively, with several Bragg spots indexed. Scale bars, 5  $\text{nm}^{-1}$  (b); 2  $\text{nm}^{-1}$  (e). (c,f) Crystal structures of (c) WSe<sub>2</sub> and (f) Ge, as viewed down the [001] and [110] zone axes, respectively. In c: yellow spheres = Se; blue spheres = W, as labelled.

major energy carriers emerging from electron–phonon coupling and reflecting the onset of coherent thermal transport. Note that GHz lattice-oscillation frequencies have also been observed in crystalline Si with an ultrafast electron microscope via femtosecond convergent-beam diffraction<sup>40</sup>.

From the image series, it is immediately apparent that the phonon wavefronts do not emerge in a spatially uniform manner. Rather, within the WSe<sub>2</sub> flake, wavetrains are nucleated at a localized region along a distinct step-edge, and the subsequent propagation direction is perpendicular to the interface (see Supplementary Video 1). The wavetrain emerges in 1 ps (see below), is launched and propagates at a velocity of 5.5  $\text{nm ps}^{-1}$  away from the step edge. In the Ge specimen, the appearance and directionality of the propagating phonon wavefronts are seen to follow existing bend contours present in otherwise pristine crystalline regions (see Supplementary Video 2). Also apparent in the video are relatively weak contrast oscillations in the upper-right portion of the frame. These oscillations occur within a relatively pristine region of the Ge specimen (that is, free of significant defects and crystal bending, as indicated by the relatively weak contrast).

**Emergence of a phonon from a step edge.** To precisely resolve the phonon dynamics at an individual step edge, image series of WSe<sub>2</sub> were acquired with increased magnification and finer temporal sampling (500-fs steps). Within the region of interest highlighted in Fig. 3, the intensity was observed to initially increase at a step edge in the first few-hundred femtoseconds and

continue to grow for approximately 10 ps before relaxation via emission of a travelling wave approximately perpendicular to the interface (see Supplementary Videos 3 and 4). The processed difference images (Fig. 3b–f; see ‘Methods’ section) and corresponding time-dependent intensity traces (Fig. 3g) display the emergence mechanism of the in-plane acoustic phonons shown in Fig. 2j–o. Notably, the frequency of dynamic intensity at the step edge is in accord with the interlayer echoing of back-and-forth acoustic phonons and resulting oscillating moiré fringes<sup>41–43</sup> (see also Supplementary Fig. 3). It is therefore likely that the differential stress imparted on the interface by dephasing of the longitudinal *c* axis waves across regions of differing height gives rise to the formation of the in-plane travelling phonons. Systematic studies to probe this and other aspects associated with the dynamic contrast mechanisms are currently in progress and will be described elsewhere.

**Spatially dependent acoustic phonon properties.** The information contained in the image series can be further illustrated via a space–time plot (see ‘Methods’ section). In Fig. 4a, an analysis of contrast dynamics observed in the region between the WSe<sub>2</sub> crystal–vacuum interface and the step edge is summarized (see also Supplementary Video 5). Each streak corresponds to one period of an acoustic phonon, with the slope and width indicative of phase velocity and frequency, respectively. Such an analysis reveals the presence of multiple modes in this region, with a relatively high-frequency oscillation (phase velocity = 5.5  $\text{nm ps}^{-1}$ ) generated during the initial moments of excitation,

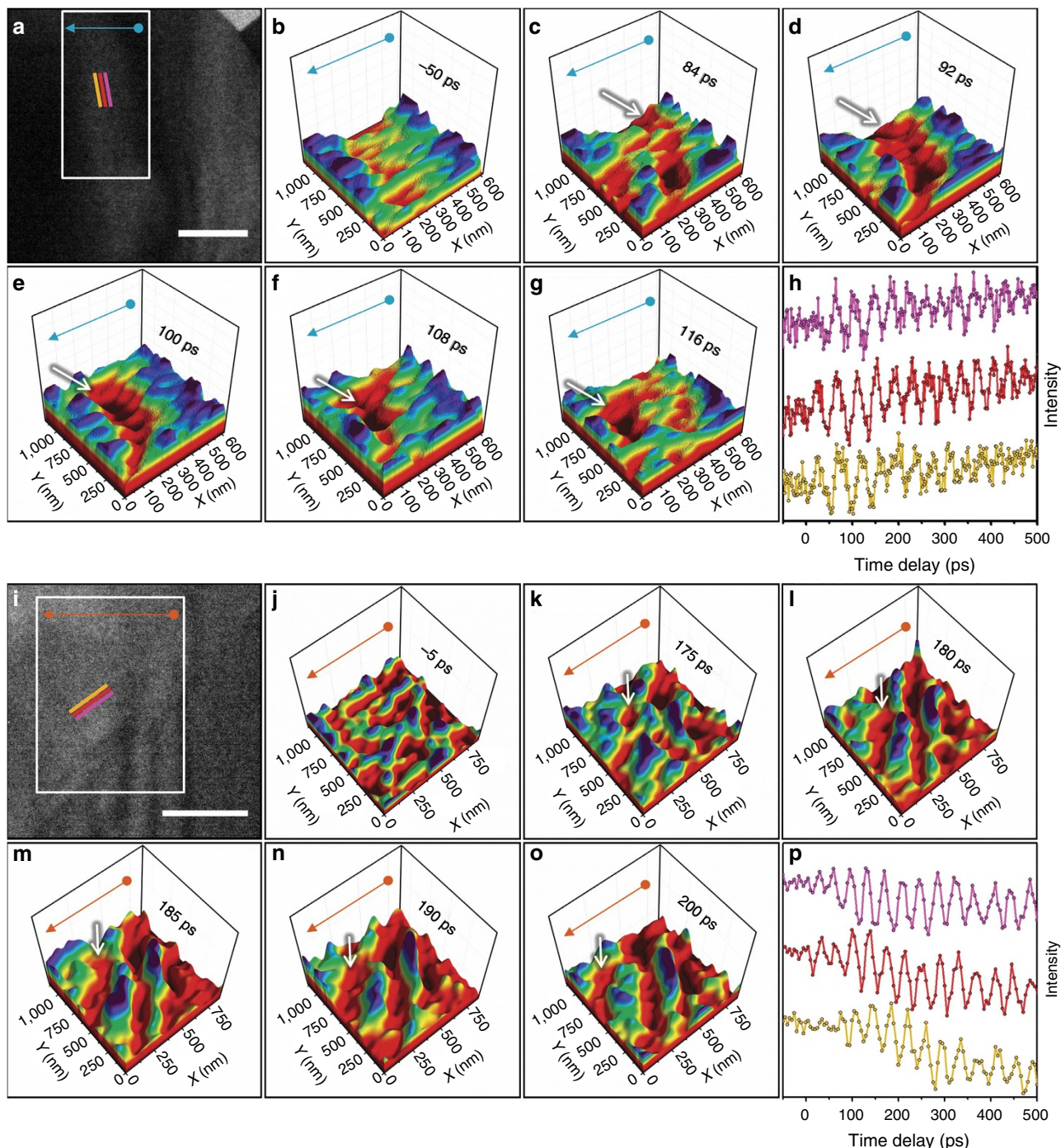


**Figure 2 | Real-space femtosecond electron imaging of single-phonon wavefronts in Ge and WSe<sub>2</sub>.** (a,i) Bright-field images of the Ge and WSe<sub>2</sub> regions shown in Fig. 1 and obtained at  $-50$  and  $-5$ -ps time delays, respectively. For the Ge experiments, the images were acquired with a 25-kHz repetition rate and a 13-s integration time per frame. For WSe<sub>2</sub>, the images were also acquired with a 25-kHz repetition rate but with an 18-s integration time per frame (see also the captions for Supplementary Videos 1 and 2 for further experimental details). The three coloured lines mark regions from which the mean intensity was quantified and used to generate the time traces in **h** and **p** (described below). The propagation direction is perpendicular to the coloured lines. Scale bars, 500 nm. (b-g) and (j-o) Surface plots generated from an image series (region of interest = white rectangles in **a** and **i**) highlighting approximately one period of wavetrain propagation, with a pre-time-zero frame included for reference. Motion of individual wavefronts, which appear as a continuous, deep-red depression, is indicated by the white arrows. The blue and orange arrows map the orientation to the two-dimensional images shown in **a** and **i**. (h,p) Image-intensity measurements, obtained at the coloured lines in **a** and **i**, as a function of time delay (offset for clarity).

and slower ( $0.9 \text{ nm ps}^{-1}$ ), lower-frequency dynamics dominating after a few-hundred picoseconds. Similar spectral features identified with Brillouin light scattering from thin silicon membranes have been attributed to Lamb-wave modes<sup>44</sup>. Analogously here, the confinement of longitudinal acoustic phonons within the

specimen thickness gives rise to in-plane propagating modes. These consist of travelling symmetric ( $S'_0$ ) and antisymmetric ( $A_0$ ) interlayer displacements (Fig. 4c). It has been predicted that such dilatational and flexural acoustic modes significantly influence thermal transport in layered materials<sup>45</sup>.

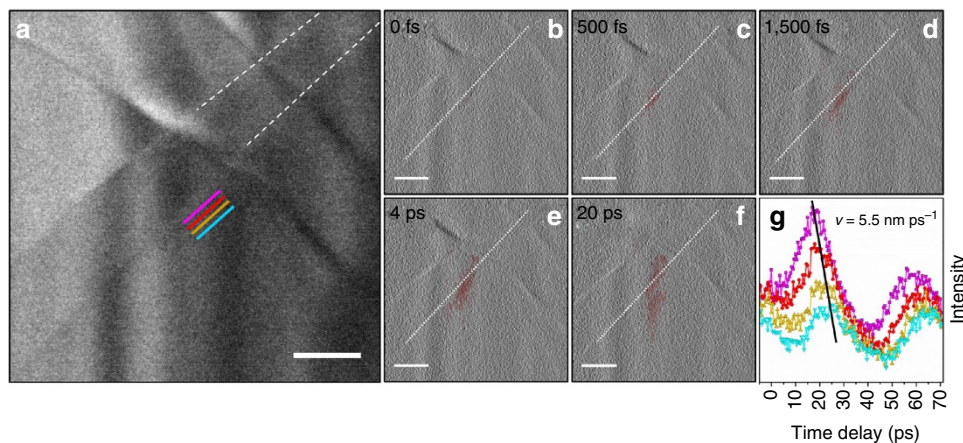


**Figure 3 | Femtosecond-resolved phonon nucleation and launch at a crystal step-edge.** (a) Bright-field image highlighting two step-edges (indicated by the partial dashed white lines) in the  $\text{WSe}_2$  flake. The coloured lines represent regions from which the mean intensity was quantified and used to generate the time traces in **g**. The images were acquired with a 50-kHz repetition rate and a 20-s integration time per frame (see also the captions for Supplementary Videos 3 and 4 for further experimental details). (b–f) Select processed micrographs revealing the nucleation and emergence of a localized phonon wavefront (red). The dotted white lines indicate the position of the step-edge from which the wavefront emerges. (g) Intensity measurements obtained at the coloured lines in **a** and plotted as a function of time delay. The slope of the line passing through the peaks of the first oscillation period reflects the wavefront velocity of  $5.5 \text{ nm ps}^{-1}$ . Scale bars, 200 nm.

Inspection of the spatial dependence of the two phonon modes illustrated in Fig. 4 via application of a discrete time-domain Fourier transform in three different spatial regions reveals that both are split into multiple branches, with the degree of excitation dependent on local morphology. A frequency trace near the crystal–vacuum interface returns dominant modes at 36 and 39 GHz (Fig. 4b, green), whereas 21 and 25 GHz are found at the step edge (Fig. 4b, red). In each case, the two dominant peaks correspond to the frequency of the back-and-forth  $c$  axis acoustic phonons ( $LA_{\text{rt}}^i$ ) and that of the resulting dilatational Lamb-wave mode ( $S_0^i$ ). Consequently, the morphologically dependent dispersion likely results from the difference in thickness between the regions from which phonons originate. In addition, the low-frequency flexural mode ( $A_0$ ) is also split into multiple branches despite emanating from a region of uniform thickness. Although this may occur from phonon interactions with bends and ripples in the flake, analysis of frequency traces obtained from the intermediate section (Fig. 4b, blue) show that the  $A_0$  mode is strongly damped upon reaching the step edge. Such dynamics are the basis of the large disparities in thermal conductivity of layered materials<sup>23,45</sup>.

## Discussion

For all the studies reported here, the laser-excitation wavelength used was 515 nm (2.41 eV). This photon energy is significantly larger than the band gaps of both  $\text{WSe}_2$  and Ge (1.6 and 0.66 eV, respectively)<sup>46,47</sup>. Accordingly, the roles played by charge-carrier excitation and recombination on localized acoustic-phonon nucleation and launch may be non-negligible. Indeed, the question of why acoustic phonons first appear at specific locations in the material is nontrivial to answer considering the sequence of events that occurs following femtosecond excitation—especially in a disordered material—and the mechanisms of contrast formation in the bright-field images (discussed below). Although this topic is the subject of current systematic studies in our lab, it nevertheless is perhaps worthwhile to draw comparisons to multi-photon pump-probe photoemission electron microscopy. In this variant of photoemission electron microscopy, resonant excitation is used to induce surface-plasmon oscillations and image their launch, propagation and evolution with

femtosecond resolution<sup>48,49</sup>. An analogous methodology dubbed photon-induced near-field electron microscopy<sup>50,51</sup>, which is not reliant on resonant excitation<sup>52–54</sup>, has recently been used to image wave-particle properties of surface plasmon polaritons and induce Rabi oscillations in swift, unbound electron packets<sup>55,56</sup>. With the resonant-excitation approach in mind, one can envision femtosecond electron imaging experiments on acoustic-phonon dynamics, where the pump-photon energy is varied with respect to the band gap of the material under study. In this way, one may be able to determine the roles played by the various dynamic and transport phenomena at work.

Beyond the acoustic-phonon excitation and nucleation mechanisms, it will be important to quantify the precise manner in which contrast is formed in the femtosecond electron images. It is well known that deviations of a few milliradians in the local Bragg condition can produce significantly different contrast patterns in bright-field micrographs. Indeed, this sensitivity to local morphology is what enables observation of dynamic contrast from small angular perturbations caused by in-plane propagating waves. It is expected that the nature of the contrast resulting from the acoustic waves is highly dependent on both vicinity to a zone axis and the specific zone axis itself. It is important to note that each of the videos of the  $\text{WSe}_2$  flake presented in this study are acquired at slightly different orientations (due to the variability of sample insertion from one experiment to the next) and in fact show noticeable differences in static diffraction contrast (compare Supplementary Videos 1 and 5). In each case, however, the waves appear to emanate from the same features, and the frequencies and phase velocities extracted are the same. Nevertheless, the exact dependence of specimen orientation with respect to specific dynamic modulations indeed is an open question (and will be the subject of a forthcoming publication).

In conclusion, we have reported the direct, real-space imaging of acoustic-phonon dynamics in macroscopically ordered but microscopically disordered crystalline  $\text{WSe}_2$  and Ge. Via femtosecond electron imaging, we have discovered that phonon nucleation and launch occurs at discrete spatial locations along individual step edges, and that the appearance of coherent, propagating wavefronts are extremely sensitive to the shapes of local strain fields (manifested in bend contours) and

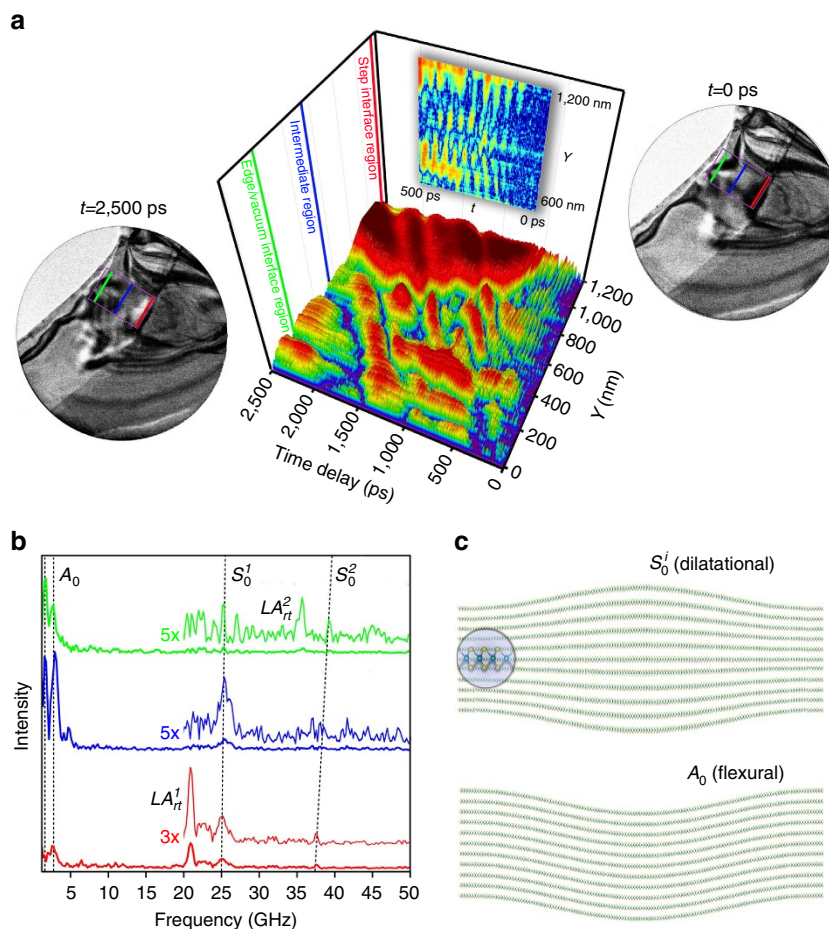


**Figure 4 | Analysis of distinct localized phonon modes in WSe<sub>2</sub>.** (a) Surface plot revealing the evolution of two primary modes, as observed in the region of interest highlighted in the accompanying images ( $t = 0$  and  $2,500$  ps; purple boxes). The images were acquired with a 25-kHz repetition rate and an 18-s integration time per frame (see also the captions for Supplementary Video 5 for further experimental details). The coloured lines demarcate the specific subregions analysed. The thin, near-vertical streaks predominantly in the sub-500-ps range and spanning the entire step interface region (600 to 1,200 nm; magnified in the inset) are produced by a relatively high-frequency mode, whereas the large amplitude, broad, diagonal features continuing out to the time-window limit are due to a more slowly propagating low-frequency mode. (b) Time-domain Fourier transform of traces obtained from the subregions marked by the coloured lines on the surface plot in **a**. The peaks arising from echoing of longitudinal acoustic phonons ( $LA_{rt}^i$ ) are labelled, while the travelling-wave modes ( $A_0$ ,  $S_0^i$ ) are indicated by the dashed lines, highlighting propagation dispersion (see also Supplementary Fig. 4, which illustrates dispersion observed in the Ge crystal, and Supplementary Video 6, which shows the effects of edge shape on the appearance of propagating diffraction contrast). The superscript  $i$  indicates waves emanating from the thicker step-edge region ( $i = 1$ ) and from that bounded by the crystal-vacuum interface ( $i = 2$ ). The spectra are offset for clarity. (c) Schematic of the symmetry of the propagating phonon modes with magnified view of a single layer. The dilatational modes ( $S_0^i$ , top) occur near 25 and 40 GHz, while the flexural modes ( $A_0$ , bottom) range from 2 to 5 GHz.

vacuum–crystal interfaces. Further, the analysis of picosecond contrast modulation reveals the phase velocities, frequencies and symmetries of the modes, with the spatial and layer-thickness dependence of the oscillations being resolved. We expect that these observations, and the method used, will open the way to the ultraprecise manipulation and control of coherent energy propagation at the atomic scale, with the possibility of exploring the spatiotemporal limits of quantized thermal energy<sup>57</sup>.

## Methods

**Specimen preparation.** The WSe<sub>2</sub> (2-H) flakes were prepared via mechanical exfoliation<sup>58</sup> of a single-crystal obtained from Nanoscience Instruments. Isolated flakes were transferred to an atomically flat, cleaved (100) NaCl substrate (Ted Pella) before a polymer support film was deposited by drop-casting 20  $\mu$ l of a solution of 2-wt% polymethyl methacrylate (PMMA) in anisole. The NaCl substrate was etched for 10 to 15 min in a de-ionized water bath, leaving the flakes supported by the PMMA film. The specimens were then positioned on a 2,000-mesh Cu TEM grid via micromechanical manipulation followed by dissolution of the PMMA support film in an acetone bath overnight.

The Ge specimen was prepared via mechanical polishing at a 2° angle from a bulk (110)-oriented, undoped wafer (MTI Corporation) followed by ion milling to electron transparency. The specimen was then epoxy bonded to a Cu slot grid. The irregularly shaped edges of the Ge specimen result from the polishing process as well as non-uniform material removal during ion milling.

**Laser parameters.** The Ge and WSe<sub>2</sub> specimens were optically excited *in situ* with a pump pulse of 270-fs duration full-width at half-maximum and centred at 515 nm (2.41 eV). The pulses were generated with a Yb:KGW (1.03  $\mu$ m fundamental), diode-pumped solid-state laser and harmonics generation module (Light Conversion; PHAROS and HIRO, respectively). The pulse duration was measured *ex situ* with an in-house-built autocorrelator. The pump fluences incident on the Ge and WSe<sub>2</sub> were 1.3 and 5.0 mJ cm<sup>-2</sup>, respectively. These fluences were calculated on the basis of a laser spot size of 100- $\mu$ m full-width at half-maximum, as measured *ex situ* with a beam profiler (Newport LBP-1) using focusing parameters identical to those along the path to the specimen region.

To generate the probing photoelectron packets, the pump line was split, and a portion of the 515-nm pulses was frequency doubled to 257.5 nm and focused into the gun region of the microscope. The experiments highlighted in Figs 2 and 4 of the main text were performed at a repetition rate of 25 kHz, while the

higher-resolution scan in Fig. 3 was performed at 50 kHz. In each case, the repetition rates were such that complete mechanical and thermal relaxation was achieved before each subsequent excitation.

**Microscope parameters.** All the experiments were performed with a Tecnai Femto ultrafast electron microscope (FEI Company) operated at 200 kV in both thermionic and photoelectron modes. In both modalities, a truncated, 150- $\mu\text{m}$  flat LaB<sub>6</sub> cathode (Applied Physics Technologies) was used. To capture the greatest number of photoelectrons at the relatively low repetition rates used here<sup>39</sup>, a custom 1,250- $\mu\text{m}$  condenser aperture was used for all the experiments. For all the bright-field experiments, a 40- $\mu\text{m}$  objective aperture was used. For all the selected-area diffraction experiments, a 200- $\mu\text{m}$  projection aperture was used, which collected electrons passing through a 20- $\mu\text{m}^2$  area. This same aperture can be seen in the bright-field-imaging Supplementary Videos 1 and 5. The images were recorded with a Gatan Orius SC200B 2,048  $\times$  2,048 CCD camera and with integration times ranging from 13 to 20 s per frame. On the basis of the total electron counts (approximately  $(1 \times 10^8)$  to  $(5 \times 10^8)$ ) acquired with the beam focused to the size of the CCD chip for a given exposure time and repetition rate, it is estimated that 200 to 1,000 electrons per pulse were used for image formation.

**Control experiments.** To exclude a host of potential artifacts and undesirable instabilities of the experimental system as the cause of the observed propagating contrast waves, a series of control experiments were performed in duplicate. These were conducted immediately after scans in which the periodic contrast was observed and using the same experimental parameters. (1) A control experiment for specimen drift/tilt was twice performed by acquiring 47 images at a fixed time delay (for example,  $-100$  ps) to replicate the duration of a full-time scan (for example, 20 min). (2) A control experiment for image fluctuations due to potential photoelectron-source instabilities was performed twice by acquiring 50 images over 20 min without specimen excitation. (3) A control experiment for beam instabilities due to movement of the delay stage was performed twice by acquiring 50 images without specimen excitation but still translating the delay stage on the laser table as if a scan (200 ps with 4-ps steps over 20 min) were being performed. (4) A control experiment for the equilibrium thermal effects of pumping the specimen was performed twice by acquiring a series of 50 images over 10 min spanning a delay range of 200 ps but using a thermionic rather than photogenerated electron beam. No propagating contrast waves—indeed, no dynamics of any kind—were observed in the controls.

**Data and image processing.** In generating panels (b–g) and (j–o) in Fig. 2 of the main text, several steps were taken in converting the photoelectron images to three-dimensional surface plots. First, difference images were created by taking an average of 10 pre-time-zero images (dubbed the reference image) and subtracting it from each frame in the series. Second, the difference image was modified for contrast and brightness to enhance the features of interest, including passing the images through a 10-pixel Gaussian smoothing filter. Third, each image was levelled by adjusting any pixels with values above 90% or below 10% of the maximum and minimum intensity, respectively, to the 90 and 10% values, respectively. In addition, a one-pixel swath along the edges of each image was set to the 10% intensity value.

The line scans shown in Fig. 2h,p of the main text were generated by first drift correcting the series of images and rotating each frame such that the direction of propagation was horizontal across the field of view. Following this, three adjacent regions measuring  $12 \times 100$  pixels were identified in each image series such that the contrast waves traversed these in succession; the regions were offset in the horizontal direction such that each would sample the contrast wave one after the other. At every time delay, each region was summed in the vertical direction, and the average was determined in the horizontal. Plotting the mean intensities as a function of time delay makes apparent the transitory nature of the waves, as illustrated in Fig. 2 of the main text. Phase velocities were extracted by taking the slope of a line connecting the peaks of the mean intensities and converting the pixel values of each region to a real-space position. The image series from which Fig. 2a–h and Fig. 2i–p of the main text were generated comprise Supplementary Videos 1 and 2.

The panels (b–f) of Fig. 3 in the main text were generated in a similar manner as Fig. 2. A 6-pixel by 6-pixel average filter was applied to difference images created by subtracting an average of 10 pre-time-zero images (that is, the average reference image). The resulting frame was then thresholded at the 80th percentile and placed in the saturation channel of an HSV (hue, saturation and value) image such that the bright, dynamic contrast appears red. To highlight the appearance of contrast at the interface, a 3-pixel by 3-pixel vertical Prewitt-filtered version of the original image was placed in the value channel. The line scans were obtained in the same fashion as for Fig. 2. The image series from which Fig. 3 of the main text was generated comprise Supplementary Video 3, while the processed images comprise Supplementary Video 4.

The space–time surface plot in Fig. 4a of the main text was generated by first rotating each image such that the axis of propagation is oriented directly vertical. A 651-pixel (Y) by 100-pixel (X) box was selected for the region of interest and median filtered (4-pixel by 4-pixel). Next, the profile for each time delay was

created by determining the mean of the 100-horizontal pixels for each of the vertical single-pixel-wide sections and then subtracting the vertical 651-pixel time-zero reference. Thus, the motion appears as diagonal streaks in the surface plot, with the velocity captured in the slope. The frequency traces were created by taking a discrete Fourier transform of a de-trended time trace for various pixels (one at a time). The displayed results represent the average of the Fourier transforms determined over the 20-pixel vertical range.

In generating panels (b–g) and (j–o) in Supplementary Fig. 1, a series of processing steps were performed, with the goal being to produce an additional means for visualizing the propagating contrast waves without the aid of the video format and within which the dynamics are readily apparent. First, the difference images were created by generating an average reference image and subtracting it from each frame in the series. Then, the difference image was modified for contrast and brightness to enhance the features of interest. Next, an HSV image was created by placing the original (at some time delay,  $t$ ) in the hue channel and the difference image (at  $t$ ) in the saturation and value channels. Finally, the colour balance was modified to emphasize the dynamic contrast. Each image within a data set was processed identically.

## References

- Dougherty, T. P. *et al.* Femtosecond resolution of soft mode dynamics in structural phase transitions. *Science* **258**, 770–774 (1992).
- Fritz, D. M. *et al.* Ultrafast bond softening in bismuth: mapping a solid's interatomic potential with X-rays. *Science* **315**, 633–636 (2007).
- Ernstorfer, R. *et al.* The formation of warm dense matter: experimental evidence for electronic bond hardening in gold. *Science* **323**, 1033–1037 (2009).
- Wall, S. *et al.* Ultrafast changes in lattice symmetry probed by coherent phonons. *Nat. Commun.* **3**, 721 (2012).
- Xi, X. *et al.* Strongly enhanced charge-density-wave order in monolayer NbSe<sub>2</sub>. *Nat. Nanotechnol.* **10**, 765–769 (2015).
- Kaasbjerg, K., Thygesen, K. S. & Jacobsen, K. W. Phonon-limited mobility in n-type single-layer MoS<sub>2</sub> from first principles. *Phys. Rev. B* **85**, 115317 (2012).
- Katayama, I. *et al.* Ferroelectric soft mode in a SrTiO<sub>3</sub> thin film impulsively driven to the anharmonic regime using intense picosecond terahertz pulses. *Phys. Rev. Lett.* **108**, 097401 (2012).
- Kampfthaler, T., Tanaka, K. & Nelson, K. A. Resonant and nonresonant control over matter and light by intense terahertz transients. *Nat. Photonics* **7**, 680–690 (2013).
- Kaasbjerg, K., Thygesen, K. S. & Jauho, A.-P. Acoustic phonon limited mobility in two-dimensional semiconductors: deformation potential and piezoelectric scattering in monolayer MoS<sub>2</sub> from first principles. *Phys. Rev. B* **87**, 235312 (2013).
- Sengupta, A., Chanana, A. & Mahapatra, S. Phonon scattering limited performance of monolayer MoS<sub>2</sub> and WSe<sub>2</sub> n-MOSFET. *AIP Adv.* **5**, 027101 (2015).
- Safavi-Naeini, A. H. *et al.* Electromagnetically induced transparency and slow light with optomechanics. *Nature* **472**, 69–73 (2011).
- Fainstein, A., Lanzillotti-Kimura, N. D., Jusserand, B. & Perrin, B. Strong optical-mechanical coupling in a vertical GaAs/AlAs microcavity for subterahertz phonons and near-infrared light. *Phys. Rev. Lett.* **110**, 037403 (2013).
- Luckyanova, M. N. *et al.* Coherent phonon heat conduction in superlattices. *Science* **338**, 936–939 (2012).
- Zebarjadi, M., Esfarjani, K., Dresselhaus, M. S., Ren, Z. F. & Chen, G. Perspectives on thermoelectrics: from fundamentals to device applications. *Energy Environ. Sci.* **5**, 5147–5162 (2012).
- Zen, N., Puurtinen, T. A., Isotalo, T. J., Chaudhuri, S. & Maasilta, I. J. Engineering thermal conductance using a two-dimensional phononic crystal. *Nat. Commun.* **5**, 3435 (2014).
- Cahill, D. G. *et al.* Nanoscale thermal transport. II. 2003–2012. *Appl. Phys. Rev.* **1**, 011305 (2014).
- Maldovan, M. Phonon wave interference and thermal bandgap materials. *Nat. Mater.* **14**, 667–674 (2015).
- Hu, Y., Zeng, L., Minnich, A. J., Dresselhaus, M. S. & Chen, G. Spectral mapping of thermal conductivity through nanoscale ballistic transport. *Nat. Nanotechnol.* **10**, 701–706 (2015).
- Joshi, G. *et al.* Enhanced thermoelectric figure-of-merit in nanostructured p-type silicon germanium bulk alloys. *Nano Lett.* **8**, 4670–4674 (2008).
- Wingert, M. C. *et al.* Thermal conductivity of Ge and Ge-Si core-shell nanowires in the phonon confinement regime. *Nano Lett.* **11**, 5507–5513 (2011).
- Tian, Z., Esfarjani, K. & Chen, G. Enhancing phonon transmission across a Si/Ge interface by atomic roughness: first-principles study with the Green's function method. *Phys. Rev. B* **86**, 235304 (2012).
- Zhao, Y. *et al.* Interlayer breathing and shear modes in few-trilayer MoS<sub>2</sub> and WSe<sub>2</sub>. *Nano Lett.* **13**, 1007–1015 (2013).
- Chiritescu, C. *et al.* Ultralow thermal conductivity in disordered, layered WSe<sub>2</sub> crystals. *Science* **315**, 351–353 (2007).

24. Rose-Petrucci, C. *et al.* Picosecond-milliangstrom lattice dynamics measured by ultrafast X-ray diffraction. *Nature* **398**, 310–312 (1999).
25. Zewail, A. H. 4D ultrafast electron diffraction, crystallography, and microscopy. *Annu. Rev. Phys. Chem.* **57**, 65–103 (2006).
26. Gaffney, K. J. & Chapman, H. N. Imaging atomic structure and dynamics with ultrafast X-ray scattering. *Science* **316**, 1444–1448 (2007).
27. Chergui, M. & Zewail, A. H. Electron and X-ray methods of ultrafast structural dynamics: advances and applications. *ChemPhysChem* **10**, 28–43 (2009).
28. Miller, R. J. D. Femtosecond crystallography with ultrabright electrons and X-rays: capturing chemistry in action. *Science* **343**, 1108–1116 (2014).
29. Baum, P., Yang, D.-S. & Zewail, A. H. 4D visualization of transitional structures in phase transformations by electron diffraction. *Science* **318**, 788–792 (2007).
30. Gao, M. *et al.* Mapping molecular motions leading to charge delocalization with ultrabright electrons. *Nature* **496**, 343–346 (2013).
31. Morrison, V. R. *et al.* A photoinduced metal-like phase of monoclinic VO<sub>2</sub> revealed by ultrafast electron diffraction. *Science* **346**, 445–448 (2014).
32. Sokolowski-Tinten, K. *et al.* Femtosecond X-ray measurement of coherent lattice vibrations near the Lindemann stability limit. *Nature* **422**, 287–289 (2003).
33. Bargheer, M. *et al.* Coherent atomic motions in a nanostructure studied by femtosecond X-ray diffraction. *Science* **306**, 1771–1773 (2004).
34. Weathersby, S. P. *et al.* Mega-electron-volt ultrafast electron diffraction at SLAC National Accelerator Laboratory. *Rev. Sci. Instrum.* **86**, 073702 (2015).
35. Zewail, A. H. Four-dimensional electron microscopy. *Science* **328**, 187–193 (2010).
36. Flannigan, D. J. & Zewail, A. H. 4D electron microscopy: principles and applications. *Acc. Chem. Res.* **45**, 1828–1839 (2012).
37. Piazza, L. *et al.* Design and implementation of a fs-resolved transmission electron microscope based on thermionic gun technology. *Chem. Phys.* **423**, 79–84 (2013).
38. Plemmons, D. A., Suri, P. K. & Flannigan, D. J. Probing structural and electronic dynamics with ultrafast electron microscopy. *Chem. Mater.* **27**, 3178–3192 (2015).
39. Schutte, W. J., De Boer, J. L. & Jellinek, F. Crystal structures of tungsten disulfide and diselenide. *J. Solid State Chem.* **70**, 207–209 (1987).
40. Yurtsever, A. & Zewail, A. H. Kikuchi ultrafast nanodiffraction in four-dimensional electron microscopy. *Proc. Natl Acad. Sci. USA* **108**, 3152–3156 (2011).
41. Barwick, B., Park, H. S., Kwon, O.-H., Baskin, J. S. & Zewail, A. H. 4D imaging of transient structures and morphologies in ultrafast electron microscopy. *Science* **322**, 1227–1231 (2008).
42. Kwon, O.-H., Barwick, B., Park, H. S., Baskin, J. S. & Zewail, A. H. Nanoscale mechanical drumming visualized by 4D electron microscopy. *Nano Lett.* **8**, 3557–3562 (2008).
43. Park, H. S., Baskin, J. S., Barwick, B., Kwon, O.-H. & Zewail, A. H. 4D ultrafast electron microscopy: imaging of atomic motions, acoustic resonances, and moiré fringe dynamics. *Ultramicroscopy* **110**, 7–19 (2009).
44. Cuffe, J. *et al.* Phonons in slow motion: dispersion relations in ultrathin Si membranes. *Nano Lett.* **12**, 3569–3573 (2012).
45. Seol, J. H. *et al.* Two-dimensional phonon transport in supported graphene. *Science* **328**, 213–216 (2010).
46. Frindt, R. F. The optical properties of single crystals of WSe<sub>2</sub> and MoTe<sub>2</sub>. *J. Phys. Chem. Solids* **24**, 1107–1112 (1963).
47. Upadhyayula, L. C., Loferski, J. J., Wold, A., Girit, W. & Kershaw, R. Semiconducting properties of single crystals of *n*- and *p*-type tungsten diselenide (WSe<sub>2</sub>). *J. Appl. Phys.* **39**, 4736–4740 (1968).
48. Kubo, A. *et al.* Femtosecond imaging of surface plasmon dynamics in a nanostructured silver film. *Nano Lett.* **5**, 1123–1127 (2005).
49. Meyer zu Heringdorf, F.-J., Chelaru, L. I., Möllenbeck, S., Thien, D. & Horn-von Hoegen, M. Femtosecond photoemission microscopy. *Surf. Sci.* **601**, 4700–4705 (2007).
50. Barwick, B., Flannigan, D. J. & Zewail, A. H. Photon-induced near-field electron microscopy. *Nature* **462**, 902–906 (2009).
51. Yurtsever, A., van der Veen, R. M. & Zewail, A. H. Subparticle ultrafast spectrum imaging in 4D electron microscopy. *Science* **335**, 59–64 (2012).
52. Flannigan, D. J., Barwick, B. & Zewail, A. H. Biological imaging with 4D ultrafast electron microscopy. *Proc. Natl Acad. Sci. USA* **107**, 9933–9937 (2010).
53. García de Abajo, F. J., Asenjo-García, A. & Kociak, M. Multiphoton absorption and emission by interaction of swift electrons with evanescent light fields. *Nano Lett.* **10**, 1859–1863 (2010).
54. Park, S. T., Lin, M. & Zewail, A. H. Photon-induced near-field electron microscopy (PINEM): theoretical and experimental. *New J. Phys.* **12**, 123028 (2010).
55. Feist, A. *et al.* Quantum coherent optical phase modulation in an ultrafast transmission electron microscope. *Nature* **521**, 200–203 (2015).
56. Piazza, L. *et al.* Simultaneous observation of the quantization and the interference pattern of a plasmonic near-field. *Nat. Commun.* **6**, 6407 (2015).
57. Mecklenburg, M. *et al.* Nanoscale temperature mapping in operating microelectronic devices. *Science* **347**, 629–632 (2015).
58. Novoselov, K. S. *et al.* Electric field effect in atomically thin carbon films. *Science* **306**, 666–669 (2004).
59. Kieft, E., Schliep, K. B., Suri, P. K. & Flannigan, D. J. Effects of thermionic-gun parameters on operating modes in ultrafast electron microscopy. *Struct. Dyn.* **2**, 051101 (2015).

## Acknowledgements

This work was supported primarily by the National Science Foundation through the University of Minnesota MRSEC under Award Number DMR-1420013, in part by a 3M Nontenured Faculty Award under Award Number 13673369, and in part by the Arnold and Mabel Beckman Foundation through a 2015 Beckman Young Investigator Award. D.A.P. acknowledges support from a Doctoral Dissertation Fellowship received from the Graduate School at the University of Minnesota. Acknowledgment is made to the Donors of the American Chemical Society Petroleum Research Fund for partial support of this research under Award Number 53116-DN17.

## Author contributions

D.R.C. performed the sample preparation, the experiments, and the analysis on Ge. D.A.P. performed the sample preparation, the experiments and the analysis on WSe<sub>2</sub>. D.J.F. oversaw the study, provided insight and guidance and aided in the interpretation and presentation of the data. The manuscript was prepared by D.R.C., D.A.P. and D.J.F. D.R.C. and D.A.P. contributed equally to the work.

## Additional information

**Supplementary Information** accompanies this paper at <http://www.nature.com/naturecommunications>

**Competing financial interests:** The authors declare no competing financial interests.

**Reprints and permission** information is available online at <http://npg.nature.com/reprintsandpermissions/>

**How to cite this article:** Cremons, D. R. *et al.* Femtosecond electron imaging of defect-modulated phonon dynamics. *Nat. Commun.* 7:11230 doi: 10.1038/ncomms11230 (2016).



This work is licensed under a Creative Commons Attribution 4.0 International License. The images or other third party material in this article are included in the article's Creative Commons license, unless indicated otherwise in the credit line; if the material is not included under the Creative Commons license, users will need to obtain permission from the license holder to reproduce the material. To view a copy of this license, visit <http://creativecommons.org/licenses/by/4.0/>